ORIGINAL ARTICLE

Effect of alloy composition and laser powder bed fusion parameters on the defect formation and mechanical properties of Inconel 625

Michael J. Benoit [1,2] · **Maciej Mazur** [1] · **Mark A. Easton** [1] · **Milan Brandt** [1]

Abstract

The objective of this study is to determine the effects of laser powder bed fusion (L-PBF) processing parameters and alloy composition on defect formation and mechanical properties of Inconel 625 (IN625). The effects of laser power and scan speed on defect formation were evaluated for two batches of IN625 powder with slightly different compositions. Cracks were observed in all processing conditions for the powder with higher levels of Si and Nb, but not in any condition for the powder with lower Si and Nb. The elimination of cracks through composition changes led to an improvement in all tensile properties, most notably an increase in elongation from 32% to 39–48%. The effect of composition on cracking was confirmed using solidification simulations for each alloy and a numerical cracking index. Porosity was found to have a non-linear relationship with the laser scan speed for both powder batches, with large pores forming for excessively high and low speeds, due to lack of fusion and unstable melt pools, respectively. Nevertheless, samples with relative densities exceeding 99.8% were produced through the selection of suitable values for laser power and scan speed. It is concluded that porosity in IN625 is sensitive to the selection of processing parameters, while composition changes within the nominal ranges for IN625 can significantly alter the crack susceptibility of the material.

1 Introduction

Laser powder bed fusion (L-PBF), also referred to as selective laser melting (SLM), is a metal additive manufacturing process in which a laser is scanned over a layer of powder in a pattern pre-determined by the final component geometry, causing localized melting and subsequent rapid solidification of the powder. After scanning the required geometry in a given layer, the powder bed is lowered by a set amount, new powder is distributed on top of the previous layer, and laser scanning of the new layer begins. The layer-by-layer approach allows for the fabrication of part geometries with high design freedom, resulting in more efficient designs and a reduction of material waste, which is particularly important for high value materials such as Ni-based superalloys [1].

The L-PBF parameters related to the volumetric energy density input influence defect formation and are, therefore, commonly subject to process optimization. The application of sub-optimal energy density can result in porosity defects, formed by gas entrapment, vaporization, and keyholing effects, or to lack of fusion voids formed by incomplete melting of the powder [2]. Although careful selection of L-PBF processing parameters and scan strategies can reduce or eliminate porosity, it may not be possible to eliminate micro-cracking through process parameter optimization alone. A number of potential cracking mechanisms associated with L-PBF processing of Ni-based superalloys have been identified in the literature, including solidification cracking (i.e., hot tearing), liquation cracking, and solid-state cracking phenomena such as ductility-dip cracking and strain-age cracking [3]. Ni-based superalloys have been reported to be acutely prone to solidification cracking during L-PBF processing, such as in the case of Hastelloy X [4], Inconel 625 [5], and Inconel 738 [6], and particularly when the alloys contain detrimental concentrations of minor alloying or impurity

✉ Michael J. Benoit
michael.benoit@ubc.ca

1 Centre for Additive Manufacturing, School of Engineering, RMIT University, Melbourne, VIC 3001, Australia

2 School of Engineering, University of British Columbia, Kelowna, BC V1V 1V7, Canada

elements such as C, Si, and Mn [7]. During the terminal stages of solidification, tensile stresses develop in the melt pool due to non-uniform thermal contraction between the melt pool and the adjacent solid material, which can pull apart the growing solid grains in the semi-solid "mushy" region. Cavities will form if this deformation cannot be compensated for by the interdendritic flow of the remaining liquid (e.g., due to reduced permeability of the mush), and these cavities can propagate into cracks due to the thermally induced stress [8]. The extent of solidification cracking is known to depend on several factors including material composition and freezing range, the amount and distribution of eutectic liquid at the end of solidification, and the solidification rate [9].

Inconel 625 (IN625) is a Ni-Cr alloy solid solution-strengthened with Mo and Nb, and has high resistance to strength loss, creep, and corrosion at elevated service temperatures, and has broad applicability in industries [10]. The literature regarding L-PBF of IN625 is inconsistent in reporting on defects, particularly micro-cracking, with some authors reporting cracking while others report defect-free parts, often with similar process parameters. For example, Carter et al. [11] investigated varying L-PBF process parameters for IN625 to identify a threshold energy density value for complete densification, but crack-free samples could not be produced. However, the cracking mechanism was not investigated and the reported material composition did not include the concentration of all potentially influential alloying elements. Mazur et al. [12] also observed cracks in IN625 samples produced by L-PBF with a range of laser powers and scan speeds. Thermodynamic simulations indicated that the observed cracking was due to a relatively high Si content in the powder (0.33 wt%), but this was not verified experimentally. Shuai et al. [5] showed that heating the substrate to 300 °C during the build could reduce, but not eliminate, micro-crack formation in IN625 during L-PBF. Nevertheless, the utility of this approach is impractical as most current commercial L-PBF systems limit build plate preheating to approximately 200 °C. Again, the reported powder composition was incomplete as the C content was not specified. Conversely, Li et al. [13] found no cracking in as-built and heat-treated IN625 samples produced by L-PBF. However, the reason for the defect-free parts is difficult to determine, since the L-PBF processing parameters were similar to those used by others in which micro-cracking was observed, and other potentially influential factors such as material composition were not comprehensively reported. Similarly, Marchese et al. [14] compared IN625 processed by L-PBF and laser directed energy deposition (L-DED), and found no micro-cracks in either process, but again the powder composition was not comprehensively specified.

Discrepancies in the solidification crack susceptibility of welded IN625 were noted by DuPont et al. [9]; IN625 is considered to have good weldability in practice, but cracks are often observed in lab tests, due to higher levels of restraint

on the solidifying metal. Furthermore, it was noted that samples of IN625 with different compositions, but still within the nominal composition limits of the alloy designation, can experience different levels of cracking. Therefore, the crack susceptibility of IN625 is sensitive to both the thermo-mechanical conditions during solidification and the specific alloy composition. No comprehensive study on the effect of processing conditions and minor changes to alloying composition has been undertaken for L-PBF of IN625. Therefore, the objective of this study is to elucidate the effects of processing conditions and alloy composition on defect formation and, consequently, the mechanical properties of IN625 produced by L-PBF.

2 Experimental

2.1 Material

Two commercially available pre-alloyed and gas-atomized IN625 powder batches were used in this work. Powder batch A had a higher Mo, Nb, and Si content compared to batch B, but a lower Cr, Fe, and Al content (Table 1). The powder composition was analyzed through peroxide fusion and inductively coupled plasma-atomic emission spectrometry (ICP-AES) analysis, and the C and S content was determined using a Leco combustion carbon analyzer. Batch A was procured from TLS Technik GmbH and powder batch B was procured from Renishaw plc. The powder particles are generally spherical, although some irregularly shaped particles are also present (Fig. 1). The measured particle size distribution (by volume) is presented in Table 2 for each powder batch. The powders did not present any difficulties during L-PBF manufacture with regards to flowability.

2.2 Sample preparation and testing

Each powder batch was dried at 100 °C for 3 h in an inert atmosphere before use. An SLM Solutions 125 system with a single 400W fiber laser was used to build all specimens in the current study. The samples were all built in an Ar atmosphere with the build plate preheated to 200 °C. A layer thickness of 0.03 mm, a hatch spacing of 0.12 mm, and a laser spot size of approximately 80 μm were used to fabricate all samples. A bi-directional "stripe" laser scan pattern was used within each layer of the samples and the orientation of this scan pattern

Table 1   Measured composition of IN625 powder batches (in wt%, bal. Ni)

	Cr	Mo	Nb	Fe	Si	Mn	Al	Ti	C
Batch A	20.30	10.60	3.84	1.31	0.33	0.09	0.04	0.01	0.02
Batch B	20.80	8.65	3.45	4.16	0.13	0.01	0.11	0.16	0.02

Table 2 Measured 10th, 50th, and 90th percentile particle size by volume for both powder batches (µm)

	D_{V10}	D_{V50}	D_{V90}
Batch A	19.2	35.3	51.6
Batch B	22.2	33.1	49.2

was rotated by 66.67° between subsequent layers. Furthermore, a *skywriting* function was used during sample fabrication, which adjusts the movement of the galvanometric scanning mirrors and coordinates them with the laser on and off signals in the SLM Solutions 125 system to ensure uniformity of energy input throughout the length of the scanned tracks [15]. A prior work has shown that *skywriting* eliminates large keyhole pores and improves mechanical properties during L-PBF of IN625, but does not reduce the crack susceptibility [12]. Prismatic $10 \times 10 \times 4 \ mm^3$ specimens were manufactured on high-density support structures. The processing parameters were adjusted in order to achieve a range of volumetric energy density (E) values:

$$E \left[J/mm^3 \right] = \frac{P}{h \cdot v \cdot t} \tag{1}$$
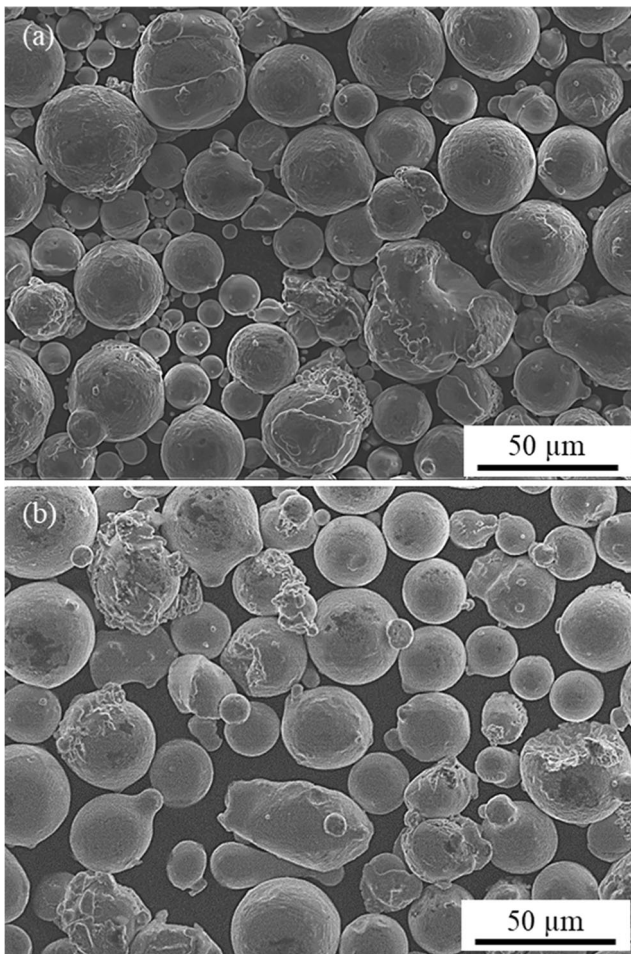
Fig. 1 Secondary electron image of IN625 powder batches (a) A and (b) B

in which P is the laser power (W), h is the hatch spacing (mm), v is the laser scan speed (mm/s), and t is the powder layer thickness (mm). The laser power was varied between 150 and 250 W, and the scan speed was varied from 415 to 1150 mm/s, in order to result in nominal volumetric energy densities of 60, 80, or 100 J/mm³ (Table 3). Samples of both powder batches were fabricated using processing conditions 1 to 9 in Table 3. After analysis of the cross sections, additional samples were fabricated using processing conditions 10 to 12 (E=40 J/mm³) with powder batch B to determine the lower limit of the processing window.

Tensile samples were printed from both powder batches using a laser power of 200 W and scan speed of 900 mm/s (Condition 2) and subsequently machined to ASTM E8 specified dimensions, with a 6-mm gauge diameter [16]. The tensile samples were printed in the vertical orientation for batch A, but in both the horizontal and vertical orientations for batch B. The samples were tested under ASTM E8 conditions using an MTS 100-kN uniaxial testing machine with a cross-head displacement corresponding to a specimen strain rate of $1 \times 10^{-3} \ s^{-1}$, and the strain was recorded with a calibrated extensometer.

2.3 Material characterization

Sample cross sections were prepared for microscopy by standard metallographic grinding and polishing, using 0.04-µm colloidal silica for final polishing. The samples were not etched prior to imaging. Optical micrographs of the sample cross sections were obtained using a Leica DM2500 light

Table 3 L-PBF processing parameters for IN625 specimens. All samples were fabricated using a layer thickness of 0.03 mm, hatch spacing of 0.12 mm, bi-directional stripe scan pattern rotated 66.67° between layers, and build plate pre-heat temperature of 200 °C. Processing conditions 1 to 9 used to print powder batches A and B, conditions 10 to 12 used to print powder batch B only

Sample no.	Power (W)	Scan speed (mm/s)	Nominal energy density (J/mm³)
1	150	690	60
2	200	900	60
3	250	1150	60
4	150	520	80
5	200	690	80
6	250	865	80
7	150	415	100
8	200	555	100
9	250	690	100
10	150	1042	40
11	200	1389	40
12	250	1736	40

microscope. Quantitative defect analysis was performed using ImageJ software to convert optical micrographs to 8-bit gray-scale images, and then applying a threshold to the micrographs to distinguish defects from the matrix. Cracks and pores were distinguished from one another by applying limits on the circularity (i.e., aspect ratio) of identified features. Circular features less than 5 μm in diameter were not included for image processing, as it was not obvious at the magnification used if these were pores or polishing artifacts. Furthermore, pores below 5 μm in diameter can typically remain present in L-PBF parts even with optimized processing parameters as reported by Kasperovich et al. [17]. Nine optical micrographs perpendicular to the build direction were used to quantify defects for each sample.

A JEOL 7200F scanning electron microscope (SEM) equipped with an Oxford Instruments X-Max 20 energy-dispersive X-ray spectroscopy (EDS) detector was used to investigate the nature of cracks in the material. Secondary electron (SE) images of the crack surfaces were captured using a working distance of 10 mm and an accelerating voltage of 5 kV, in order to minimize the interaction volume and maintain good resolution of the crack surface features. A backscatter electron (BSE) detector was also used to image the microstructure. Element maps of the crack surfaces were obtained by increasing the accelerating voltage to 8 kV and using an acquisition time of 30 min. Electron backscatter diffraction (EBSD) was performed on cross sections parallel to the build direction, in order to elucidate the relationship between crack locations and the grain structure. EBSD orientation maps were obtained with the JEOL 7200F system and an Oxford Instruments Nordlys detector, using an accelerating voltage of 20 kV, a beam current of 35 nA, a working distance of 12.6 mm, and step sizes of 1 μm for low-magnification maps and 0.5 μm for higher magnification maps. The EBSD data was post-processed using Oxford HKL CHANNEL 5 software.

2.4 Solidification simulations

The computational thermodynamic software Thermo-Calc was used to simulate the solidification behavior of IN625 alloys with varying levels of alloying elements. The simulations were performed using the Ni-based superalloy TCNI8 database and the Scheil-Gulliver solidification module, which assumes that (i) diffusion does not occur in the solid phase; (ii) there is complete mixing within the remaining liquid; and (iii) the solid-liquid interface is in equilibrium, allowing the local compositions to be estimated by the equilibrium phase diagram. DuPont et al. [9] noted that solid-state diffusion of substitutional alloying elements in Ni can be assumed to be negligible during rapid solidification, and therefore the Scheil model can be used to approximate solute distribution. However, it was also noted that dendrite tip undercooling

can occur for high energy density processes such as L-PBF, reducing the extent of microsegregation from the predicted values. Solidification simulations were performed using the compositions of powder batches A and B listed in Table 1. In addition, a 3^3 factorial design was used to determine the effect of changing Nb and Si content on the solidification behavior of IN625. In the simulations, Nb was varied between 3.5 and 4.0 wt%, Si varied between 0.0 and 0.5 wt%, and all other elements were set to the values of powder batch A. Nb and Si were selected for the simulations as they have been reported by Cieslak [18] to have a detrimental effect on solidification cracking, particularly when they are present together. The simulation data was also used to predict the effect of the alloy composition on the relative susceptibility to solidification cracking, which will be further discussed in section 4.1.1.

3 Results

Representative micrographs of cross sections perpendicular to the build direction for samples A1 to A9 are presented in Fig. 2 as a function of laser power and volumetric energy density. Cracks can be seen in each micrograph for powder batch A. However, no obvious difference in the extent of cracking can be seen for the different samples based on inspection of the micrographs. Conversely, a clear difference in the level of porosity can be seen for the different samples. Several pores with a diameter of ~50 μm or larger can be seen in samples produced with a volumetric energy density of 100 J/mm^3, particularly for the lower laser power conditions. Representative cross sections for powder batch B are presented in Fig. 3 for all processing conditions. In stark contrast to powder batch A, no cracks are visible in the micrographs for powder batch B for any of the processing conditions studied. Similar to batch A, large and relatively round pores are apparent in batch B samples processed at 100 J/mm^3, particularly with a laser power of 150 W and scan speed of 415 mm/s. Irregularly shaped pores can also be seen throughout the samples produced with an energy density of 40 J/mm^3, regardless of the laser power. The quantitative image analysis results for all samples in Figs. 2 and 3 are presented in Fig. 4, in which each data point is the average value across nine micrographs, and the error bars correspond to one standard deviation. The average level of cracking for powder batch A tends to decrease with increasing energy density for a constant laser power (Fig. 4a). Alternatively, cracking increases with increasing scan speed for a given laser power (Fig. 4b). The maximum crack area of 1.06% occurred for sample A3 ($E = 60$ J/mm^3, $v = 1150$ mm/s), while the minimum level of cracking of 0.04% occurred for sample A9 ($E = 100$ J/mm^3, $v = 690$ mm/s). The relationship between porosity and scan speed is similar for both powder batches (Fig. 4c), but the measured porosity tends to be greater for batch B than batch A at low scan

Fig. 2 Representative optical micrographs perpendicular to the build direction for powder batch A as a function of laser power and the volumetric energy density. The laser scan speed (mm/s) is displayed in the bottom left of each micrograph
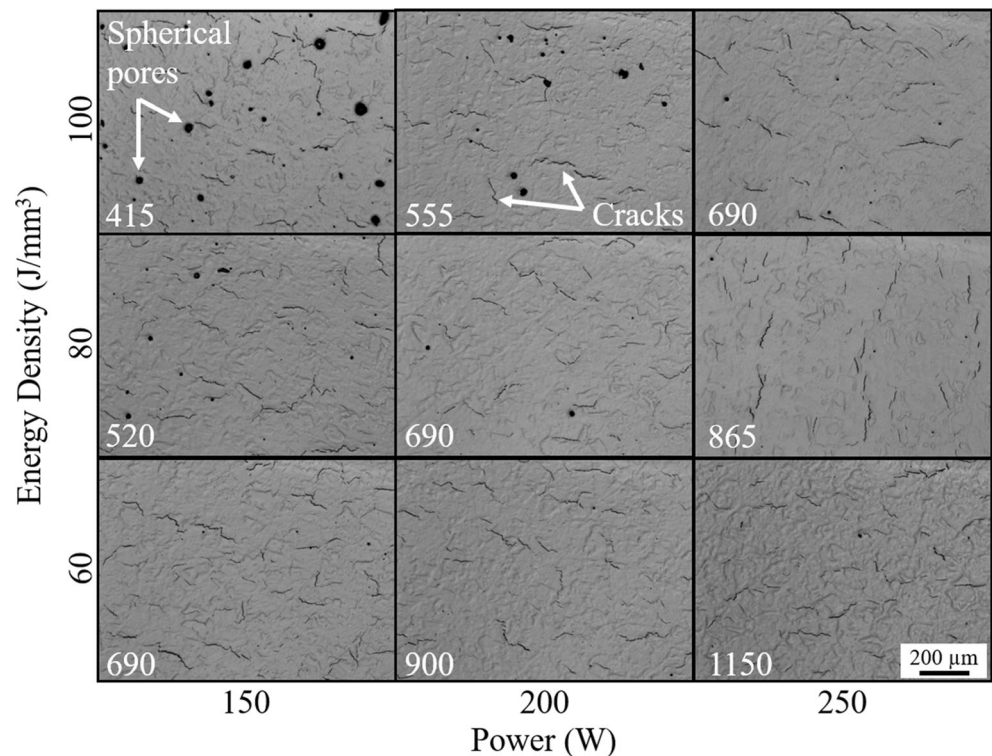
speeds. The highest levels of porosity of 1.14% and 2.71% were observed for samples A7 and B7, respectively ($E = 100$ J/mm^3, $v = 415$ mm/s). The amount of porosity rapidly decreases with increasing scan speed; samples with less than 0.2% porosity were produced with both powder batches using scan speeds between 600 and 1200 mm/s. However, the porosity in batch B again increased to between 0.7 and 0.9% when the scan speed was further increased to produce samples with an energy density of 40 J/mm^3, due to the formation of large irregular pores.

SEM-SE images of cracks along the build direction in sample A3 can be seen in Figs. 5 and 6. A columnar dendritic solidification structure can be seen in the crack opening for both cases, which is known to be a feature of solidification cracking. Furthermore, EDS element maps reveal localized enrichment of Cr, Nb, and Si on the surface of both cracks.

A SEM-BSE image of the microstructure parallel to the build direction for sample A3 can be seen in Fig. 7a. Microsegregation and submicron porosity can be seen in the higher magnification image of one of the grains in Fig. 7b. As noted by Marchese et al. [19] and Chauvet et al. [20], the distance between parallel lines of microsegregation is equivalent to the primary dendrite arm spacing (PDAS). The discontinuous nature of the microsegregation is in agreement with the phase field model predictions of Keller et al. [21], in which Nb-enriched undercooled liquid in the intercellular regions becomes "pinched off" to form discrete disk-shaped Nb-rich particles. The average measured PDAS ($n=3$ grains) was found to decrease with increasing laser scan speed (Fig. 7c).

The cooling rate during solidification can also be estimated from the PDAS measurements according to:

$$PDAS = a\left(\frac{dT}{dt}\right)^{-b} \qquad (2)$$

in which dT/dt is the cooling rate and a and b are material constants. The calculated cooling rate as a function of laser scan speed is plotted in Fig. 7c using values of $a = 50$ μm and $b = 1/3$ [19]. The error bars on the cooling rate data points correspond to the range of calculated cooling rates calculated using the average PDAS ± 1 standard deviation; due to the non-linear nature of Eq. (2), the upper and lower error bars are not equal. While significant overlap of the error bars is evident, the average cooling rate can still be seen to increase with increasing scan speed for a constant laser power, as expected. Moreover, the calculated cooling rates are all of the order of 1.0×10^5 °C/s, which is in good agreement with estimated cooling rates for L-PBF of Ni superalloys as reported by Li et al. [13].

The grain structure along the build direction of sample A3 can be seen in the EBSD orientation maps in Fig. 8. The microstructure is comprised of columnar grains aligned along the build direction. A preferred texture in the grain orientation was not readily observed. Epitaxial growth of the columnar grains across multiple build layers is fairly obvious; several grains in Fig. 8 have a length in the order of a few hundred microns, whereas the powder layer thickness was only 30 μm, so the columnar grains have grown from grains of previously solidified layers. Several cracks were also identified in each

Fig. 3 Representative optical micrographs perpendicular to the build direction for powder batch B as a function of laser power and the volumetric energy density. The laser scan speed (mm/s) is displayed in the bottom left of each micrograph
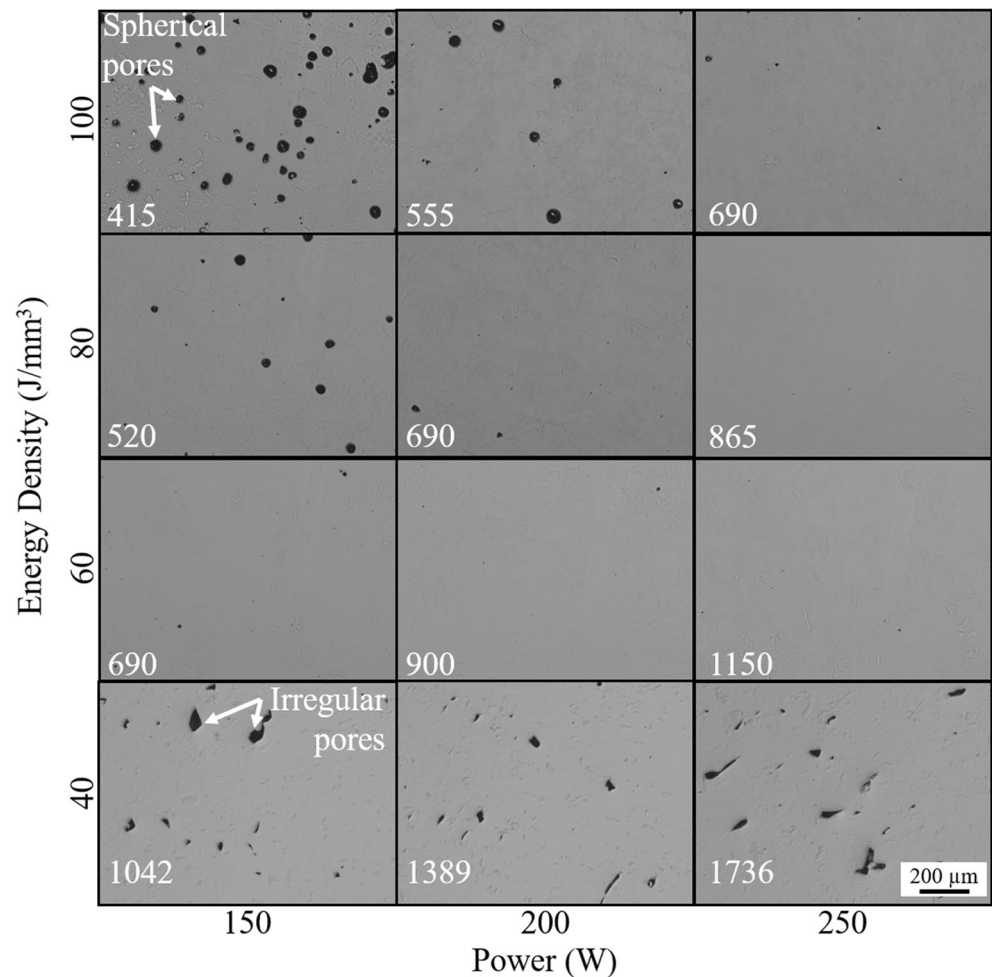
map, as the crystal orientation of these regions could not be indexed during data collection. All cracks were observed to form along high-angle boundaries, which is characteristic of solidification cracking.

A comparison of the tensile properties between powder batches A and B can be seen in Fig. 9. Powder batch B tensile samples exhibited improved tensile properties compared to batch A and match the properties of wrought IN625. Compared to sample A2, the yield and ultimate tensile strength exhibited modest increases of between 7–14% and 2–10%, respectively, while the elongation increased from 32 to 39% (B2-H) and 48% (B2-V). The increase in the tensile properties is due to the elimination of micro-cracks in batch B samples. A small amount of anisotropy can also be seen by comparison of tensile specimens manufactured in horizontal and vertical orientations with batch B. Horizontal samples exhibited a higher yield and tensile strength compared to vertical samples, but with reduced ductility. Similar results have been observed by Deng et al. [22] in as-built Inconel 718 L-PBF components, in which anisotropy in mechanical properties was attributed predominantly to differences in residual stress; higher residual stresses in the horizontal samples acted

to strengthen the microstructure in the loading direction while reducing ductility. However, a stress relief heat treatment decreased the anisotropy in mechanical properties. A similar mechanism is expected to be the cause of anisotropy between batch B horizontal and vertical tensile samples in this study. Batch A tensile samples in the horizontal orientation were not tested, as it is expected that they would have significantly lower mechanical properties compared to vertical samples, since the orientation of the micro-cracks would be perpendicular to the loading direction.

4 Discussion

4.1 Cracking

4.1.1 Composition effects

An obvious difference in the level of cracking was noted between the two powder batches in the current study (Figs. 2 and 3), despite both powder batches being within the IN625 composition limits. Cracks were observed for all processing
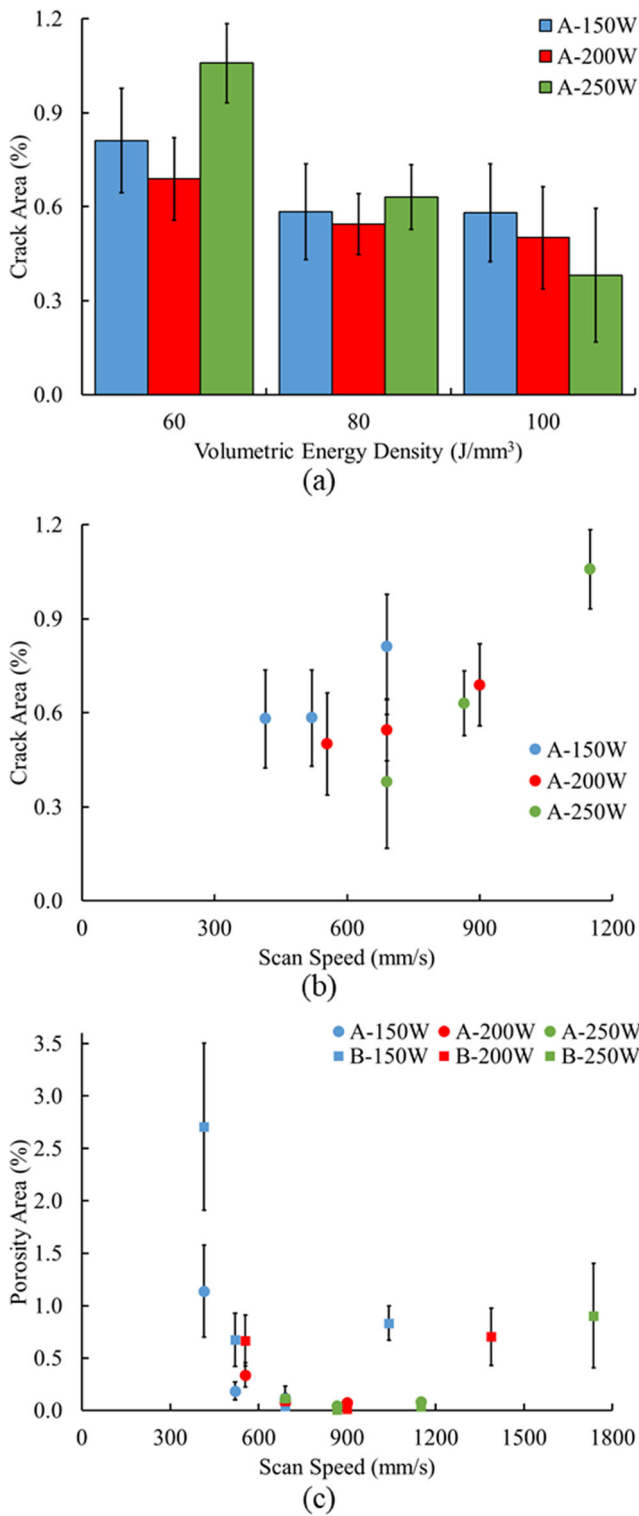
Fig. 4 Image processing results showing (a) the effect of volumetric energy density and laser power on cracking in powder batch A, (b) the effect of scan speed on cracking in powder batch A, and (c) the effect of scan speed and laser power on porosity in powder batches A and B

conditions with powder batch A, but not for any conditions with powder batch B. DuPont et al. [9] noted that slight differences within the standard alloy designation composition

ranges can lead to distinct differences in the observed level of cracking during welding of Ni-based alloys. Engeli et al. [23] also showed a distinct difference in the level of cracking during L-PBF of 8 different batches of IN738LC powder, in which the level of cracking was well correlated with the varying Si contents of the powder batches.

The compositions of the two powder batches used in this study are slightly different, including lower levels of both Nb and Si in batch B (Table 1). The connection between the alloy composition and crack susceptibility can be explained through the phases which form at the terminal stages of solidification. As noted by DuPont et al. [24], the brittle Laves phase forms at the end of solidification in Ni-based alloys with high levels of Nb and Si, due to their segregation to the interdendritic regions. Localized enrichments of Nb, Si, and Cr were observed on the dendritic crack surfaces in powder batch A (Figs. 5 and 6), which are likely the Laves phase. Cieslak [18] noted the presence of Nb, Cr, and Si in the Laves phases associated with hot cracks in welded IN625, while Dubiel and Sieniawski [25] identified a Laves phase in additively manufactured IN625 containing Nb and Cr, but interestingly, no Si.

The Thermo-Calc-predicted effect of composition on the solidification path of powder batches A and B is given in Fig. 10a, in which the overall solidification behavior is represented by the temperature vs. solid fraction (T vs. f_s) curve. It can be seen from the figure that the overall solidification temperature range is greater for batch A than batch B, and that there is a large temperature drop for $f_s \geq 0.98$ for batch A. The simulated effect of systematically varying the Nb and Si content of powder batch A is shown in Fig. 10b. It can be seen from the figure that increasing the Nb level from 3.5 to 4.0 wt% shifts the T vs. f_s curve to higher temperatures, although the effect is relatively small. Conversely, increasing the alloy Si content from 0.0 to 0.5 wt% shifts the T vs. f_s curve to lower temperatures and leads to a large temperature drop at the end of solidification. Therefore, the difference in solidification behavior of powder batches A and B is predicted to be attributed to the higher Si content of batch A.

An index developed by Easton et al. [26] can be used to further assess the effect of Nb and Si content on the relative solidification crack susceptibility of IN625. The crack susceptibility indicator (CSI_E) can be calculated from the predicted T vs. f_s curve for each composition according to:

$$CSI_E = \int_{T_0}^{T_{co}} f_s(T)\, dT \qquad (3)$$

in which T_0 is the temperature corresponding to dendrite coherency, the solid fraction ($f_{s,0}$) during solidification when the dendrites begin to impinge upon one another and the mushy zone is formed, and T_{co} is the temperature corresponding to coalescence, the solid fraction ($f_{s,co}$) when the solid grains are sufficiently interconnected such that the network
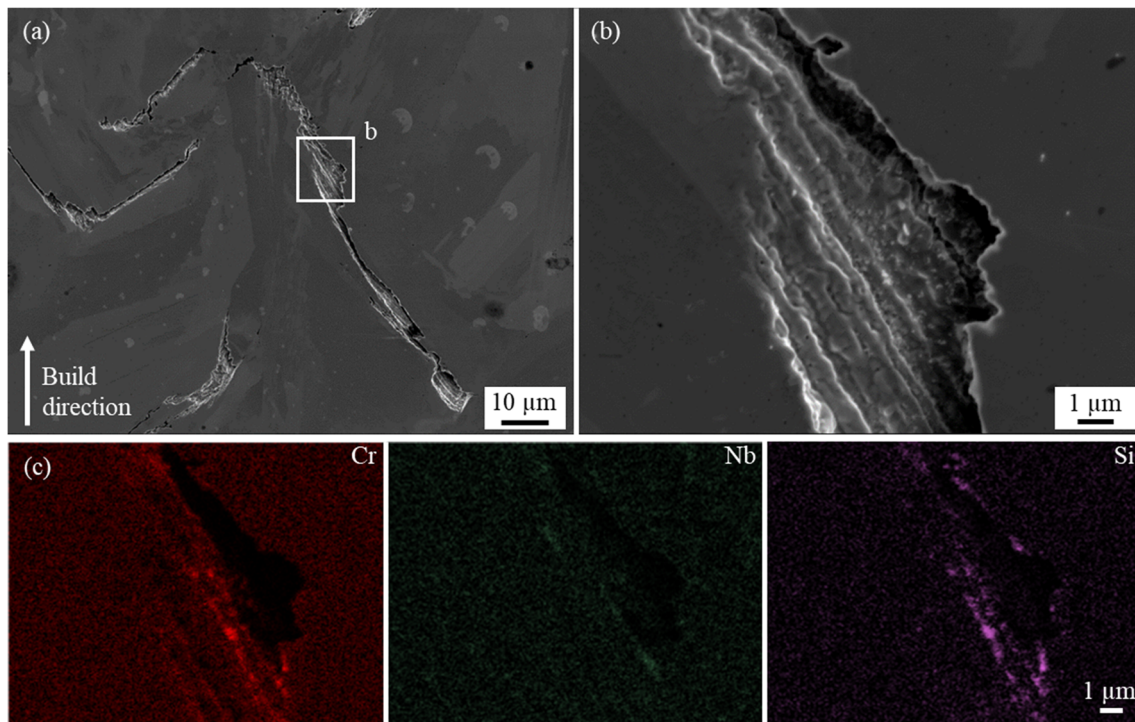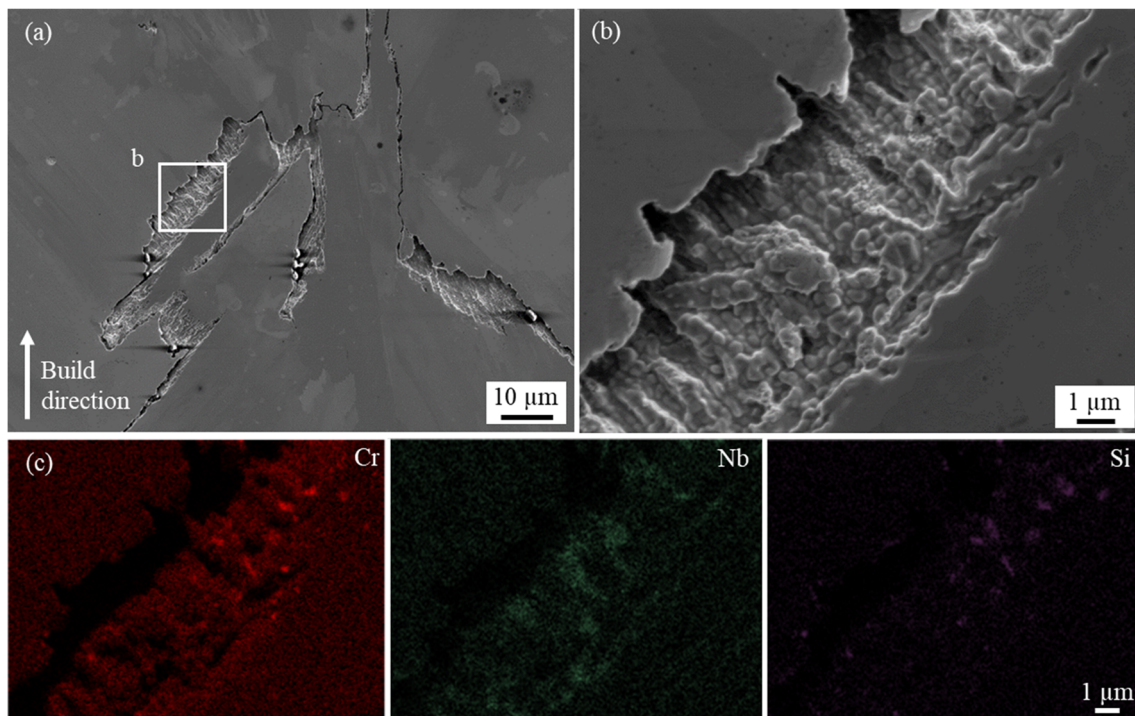
Fig. 5 (a) SEM-SE image of cracks along the build direction for sample A3 (P=250 W, v=1150 mm/s), (b) higher magnification image of region labelled "b" in (a), and (c) EDS elemental mapping of the crack surface area in (b) showing localized enrichment of Cr, Nb, and Si

behaves as a solid. Physically, CSI_E corresponds to the interval during which the alloy is considered to be in the mushy state, where the alloy is susceptible to cracking due to reduced liquid feeding through the increasingly connected dendritic structure. A larger CSI_E value indicates a greater interval in the mushy state and, therefore, greater crack susceptibility. The CSI_E values for powder batches A and B, as well as the 9 variants of batch A with varying Nb and Si contents, are

Fig. 6 (a) SEM-SE image of additional cracks along the build direction for sample A3 (P=250 W, v=1150 mm/s), (b) higher magnification image of region labelled "b" in (a), and (c) EDS elemental mapping of the crack surface area in (b) showing localized enrichment of Cr, Nb, and Si
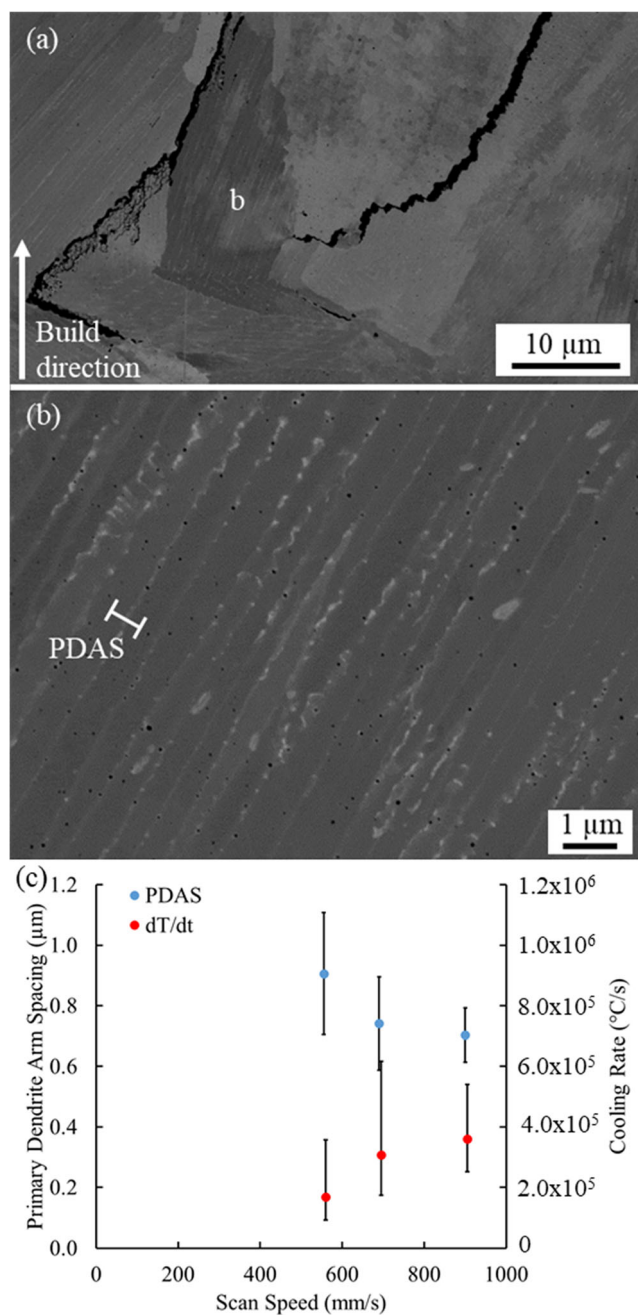
Fig. 7 SEM-BSE image of (a) sample A3, (b) higher magnification image of the grain labelled "b" in (a), and (c) the average PDAS and corresponding cooling rate (dT/dt) as a function of laser scan speed (n=3 grains, P= 200 W). Error bars are equal to 1 standard deviation for PDAS measurements and to the calculated cooling rates using the average PDAS ±1 standard deviation

plotted in Fig. 11. In the calculations, coherency and coalescence have been assumed to occur at $f_{s,0}$=0.900 and $f_{s,co}$=0.990, based on the limits applied in a similar analysis by Tomus et al. [7] for L-PBF of Hastelloy X. It can be seen from Fig. 11 that the predicted tendency to solidification cracking is greater for batch A than batch B, which is in agreement with the experimental results. The figure also clearly

demonstrates a positive correlation between increasing crack susceptibility and Si content, which was also found for L-PBF of IN738LC [23]. In addition to extending the final solidification interval when liquid feeding is restricted in the mushy zone, higher Si levels lead to the formation of the Laves phase at ~1150 °C [18]. It is proposed that the presence of the Laves phase further contributes to increased crack susceptibility by (i) embrittling the mushy zone and (ii) further reducing the permeability of the mush, exacerbating the liquid feeding issue. This appears to be reasonable, given the presence of localized Si, Nb, and Cr enrichments observed on the crack surfaces. The influence of the Nb content on the crack susceptibility is not as obvious from Fig. 11. Cieslak [18] noted that there was a small positive correlation between Nb content and crack susceptibility of IN625, but this effect was determined through comparison of a sample containing 3.6 wt% Nb and a Nb-free sample; the effect of Nb content is not as obvious when smaller differences are considered (i.e., between powders A and B). Nevertheless, the interaction between Si and Nb on crack susceptibility which was noted by Cieslak [18] can also be seen in Fig. 11 by the intersection of the trendlines for different Nb contents as the Si content increases; the solidification cracking tendency rapidly increases as Si and Nb increase simultaneously. This is a reasonable prediction, as Ni-based alloys with high Nb and Si but low C have a large mushy region, which leaves the alloy susceptible to the propagation of cracks [24].

It should be noted that the CSI_E results must be carefully interpreted. First, the indicator does not suggest a threshold value below which cracking does not occur. Powder batch B was found to be crack-free for all processing conditions in this study, while cracks were observed in all conditions with powder batch A. The CSI_E for powder batch A is 142.7 °C and 105.8 °C for powder batch B (i.e., a reduction of 25.9%). Therefore, it is expected that crack-free samples can be obtained for alloy compositions resulting in a CSI_E between these limits, but it is not clear what the threshold value is. At the present time, the indicator can only provide a relative assessment of the effect of alloy composition on cracking susceptibility. Second, it should be noted that the results of this indicator are sensitive to the selected integral limits [26]. For example, the increasing trend in CSI_E with increasing Si (and to a lesser extent increasing Nb) for the nine hypothetical alloys remains the same for $f_{s,co}$ values of 0.980 or 0.990 (although the absolute value of the integral increases with increasing $f_{s,co}$). However, when $f_{s,co}$ is selected to be 0.980, the calculated CSI_E for batch A is lower than that for batch B, which is in disagreement with the experimental results. The sensitivity to $f_{s,co}$ is related to the shape of the T vs. f_s curve at the end of solidification and the corresponding change in the integration range of the index. It can be seen from Table 4 that the temperature range over which CSI_E is calculated is more sensitive to changes in $f_{s,co}$ for powder batch A than batch B.
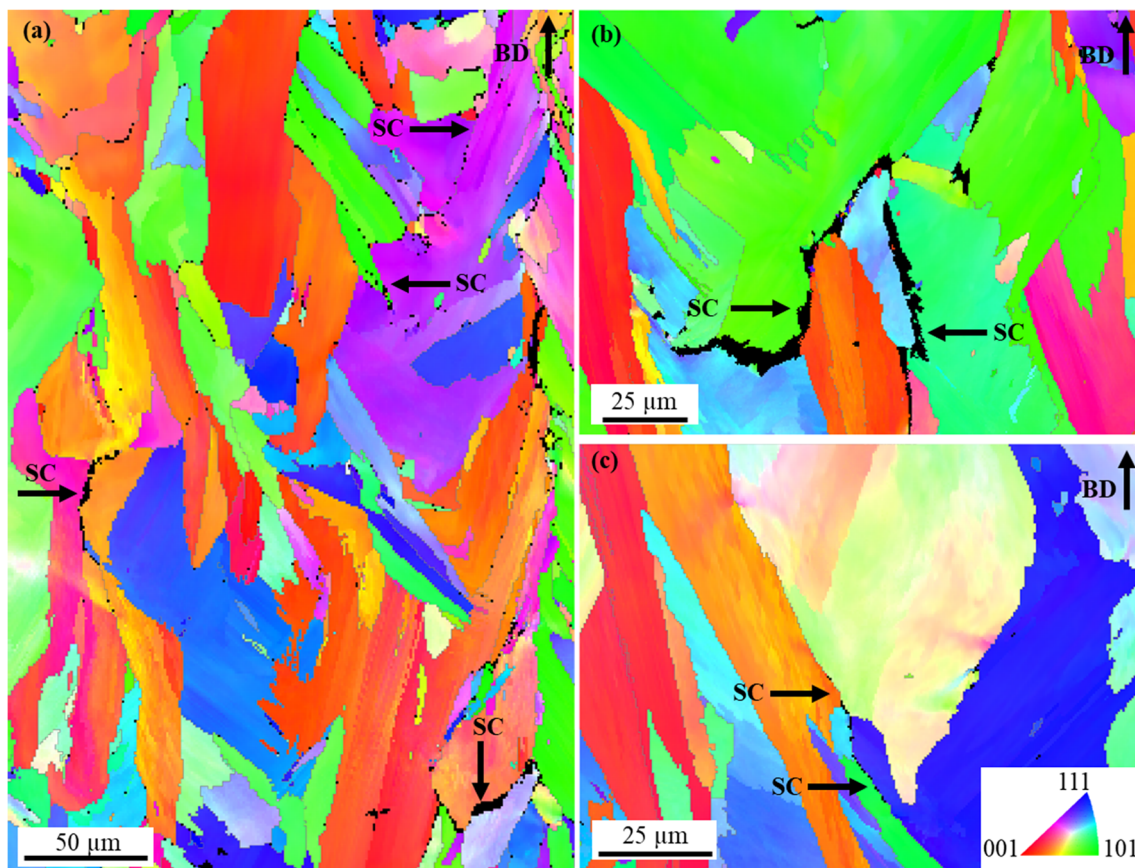
Fig. 8 EBSD orientation maps of sample A3 taken along the build direction (BD) showing several solidification cracks (SC) occurring along grain boundaries. Inverse pole figure (IPF)-Y color scheme used

The temperature drop at the end of solidification observed in Fig. 10a for powder batch A is not included in the integral when $f_{s,co}$ is 0.980, so CSI_E for batch A is less than that for batch B. However, when $f_{s,co}$ is selected to be 0.990, the temperature drop for batch A is within the integral, and the CSI_E value exceeds that of batch B.

4.1.2 Process parameter effects

Cracks were present in the micrographs for all samples of powder batch A, and Fig. 4a and b indicate that cracking also depends on the selection of processing parameters. The level of cracking was highest when the volumetric energy density was 60 J/mm^3, but no clear difference in cracking was noted between samples produced with 80 or 100 J/mm^3. Yang et al. [27] found that cracking increased with increasing energy density, and DuPont et al. [9] noted that less cracking is expected for low heat input conditions during welding of Ni-based superalloys, as the resultant mushy zone and solidification shrinkage should be lower. However, Carter et al. [11] found that evaluating cracking based on energy density alone is relatively limited, and the effect of individual processing parameters should be considered instead.

Comparison of samples fabricated with similar scan speeds but different laser powers suggests that the average measured crack area decreases with increasing laser power; this is particularly evident for samples fabricated with a scan speed of 690 mm/s. However, there is considerable variability in the crack area measurements, with error bars overlapping for samples fabricated with comparable scan speeds. The current findings are in agreement with Qiu et al. [6], who noted that cracking during L-PBF of IN718LC decreased with increasing laser power, but Yang et al. [27] showed an increase in cracking with increasing power for direct laser fabrication of Rene 104. Nevertheless, both studies noted that the level of cracking was less sensitive to laser power compared to other parameters, such as hatch spacing and scan speed.

Increasing the scan speed tended to increase the average level of cracking for a constant laser power in the present study (Fig. 4b). The reported effect of scan speed on cracking in the literature of L-PBF Ni superalloys is not consistent. Carter et al. [3] and Cloots et al. [28] both reported higher levels of cracking at low scan speeds, which was attributed to deep keyhole profiles in the later study. Conversely, a positive correlation between cracking and scan speed has been reported by Qiu et al. [6]. Kumar and Farah [29] attributed higher level of cracking at higher scan speeds to higher
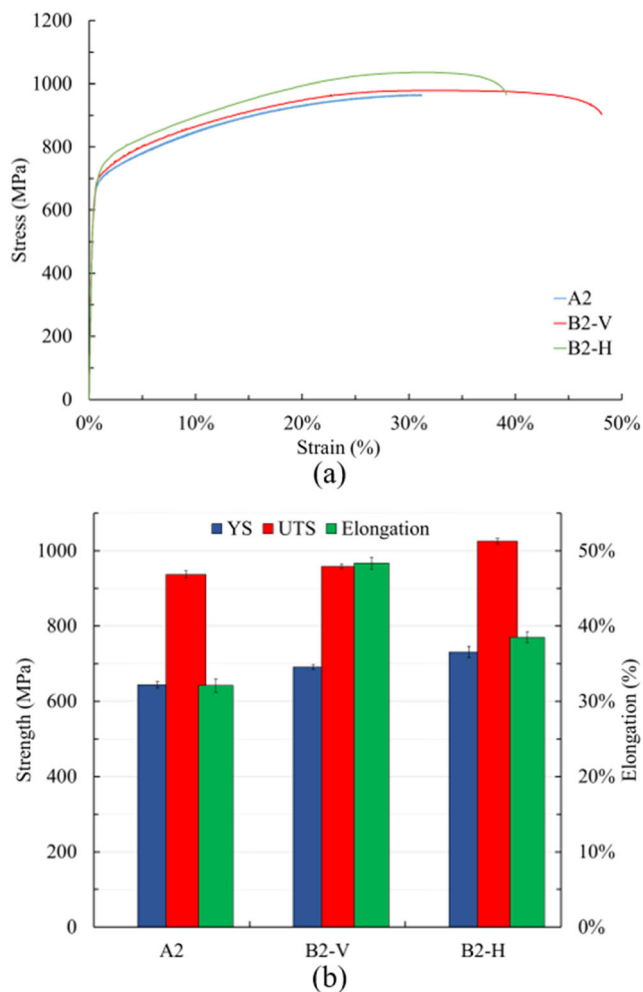
Fig. 9 (a) Representative stress-strain plots and (b) average tensile properties (*n*=3) for powder batches A and B printed using sample condition 2 in Table 3
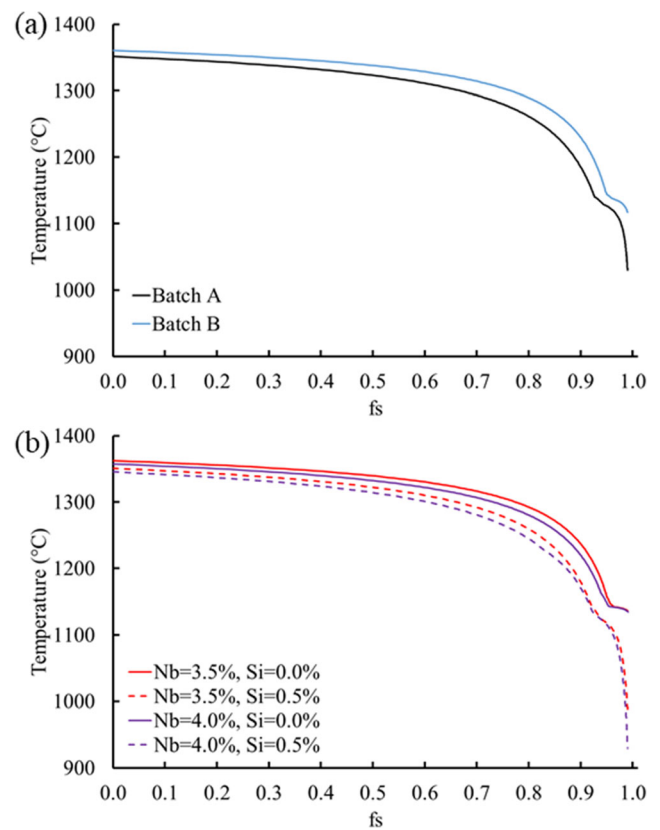

Fig. 10 Thermo-Calc-predicted T vs. f_s curves for (a) powder batches A and B and (b) powder batch A with varying Nb and Si contents (wt%)

cooling rates, which is in agreement with the PDAS measurements in Fig. 7c. DuPont et al. [9] also noted that high scan speeds can lead to centerline cracking in welding of Ni-based superalloys, due to the formation of a "tear drop"–shaped melt pool.

4.2 Porosity

The trend in the porosity vs. the laser scan speed was the same for both powder batches, although the porosity at low scan speeds was found to be greater for batch B. However, the effect of powder batch on porosity is not considered further, since near full density samples of batch B were achieved through process parameter optimization, so the remainder of this section will focus on the general relationship between scanning speed and porosity for both powder batches.

Large, irregularly shaped pores were observed in samples produced with an energy density of 40 J/mm^3, which corresponds to high scan speed conditions. The formation of non-spherical pores at high scan speeds is the result of insufficient heat input to fully melt and consolidate the powder, leading to lack of fusion defects [29]. As the scan speed was reduced and the energy density input increased, the porosity decreased and near fully dense samples were achieved, with only small spherical pores less than 5 µm in diameter observed in the micrographs (Fig. 7b). Finally, a rapid increase in porosity was noted as the scan speed was further reduced, particularly when a laser power of 150 W was used. Carter et al. [11] proposed that increasing porosity at high energy densities may be attributed to overmelting of the powder or substrate, turbulence of the melt pool, or evaporation. However, it can be seen that for the samples produced at 100 J/mm^3, the level of porosity also depends on the laser power. The samples produced using 100 J/mm^3 and 250 W have relatively low porosity, indicating that the observed porosity is more sensitive to scan speed than the overall heat input. Therefore, the large pores observed for samples fabricated with high energy density but low scan speed are attributed to instability of the melt pool, which in turn can lead to irregular melting along the track [29].

Fig. 11 Calculated CSI_E values based on the Thermo-Calc-predicted T vs. f_s curves as a function of Si for alloys with varying Nb and Si contents ($f_{s,0}$=0.900, $f_{s,co}$=0.990)
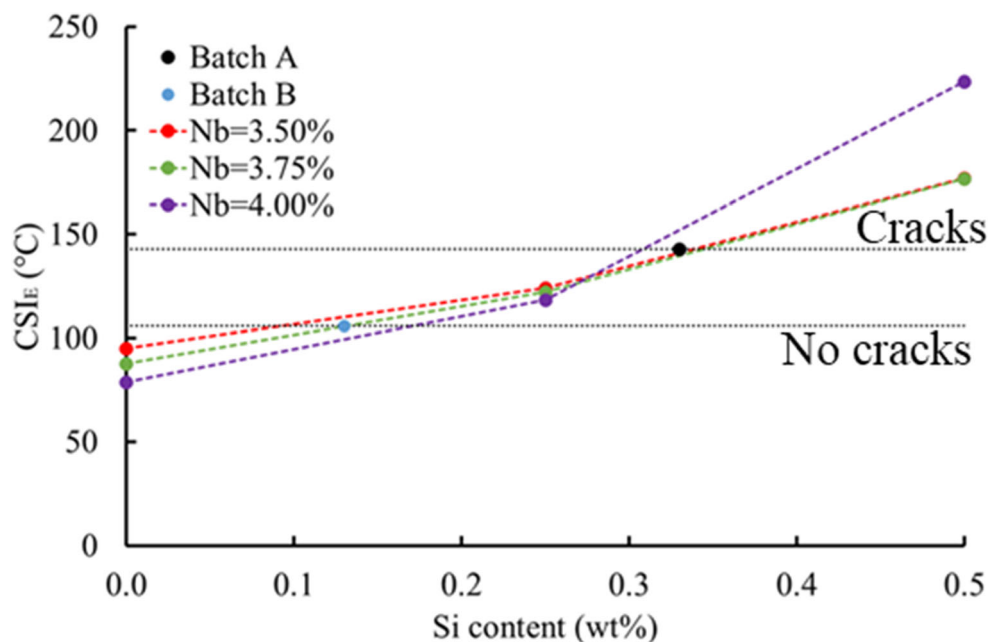
5 Conclusions

The effects of processing conditions and alloy composition on defect formation and mechanical properties of IN625 processed by L-PBF were investigated. The following conclusions can be drawn from the results:

1. The amount and nature of pores are dependent on the laser scan speed. Large and irregularly shaped pores occurred for high scan speeds due to lack of fusion. Large spherical pores were observed when the scan speed was relatively low and were attributed to irregular melting by an unstable melt pool. Samples of both powder batches with < 0.2% porosity were fabricated using scan speeds between 600 and 1200 mm/s for all laser powers.

2. Solidification cracking of IN625 during L-PBF is sensitive to the material composition, even within the nominal composition ranges of the alloy. Cracks were present in all processing conditions for powder batch A, which had a higher level of both Si and Nb compared to batch B. Analysis of the crack surfaces suggests that high Si and Nb content leads to the formation of the brittle Laves phase at the end of solidification. Moreover, the temperature range over which strain can accumulate in the mushy

zone during solidification is extended with higher levels of Si and Nb. Elimination of solidification cracks resulted in improved tensile properties, most notably an increase in elongation from 32% for batch A to 39–48% for batch B.

3. The extent of solidification cracking depends on the processing parameters, but to a lesser degree than on alloy composition. Cracking was observed to occur in all processing conditions for powder batch A, showing a positive correlation with scan speed.

Table 4 Thermo-Calc-predicted temperature difference between T_0 and T_{co} for $f_{s,co}$ values of 0.980 and 0.990 ($f_{s,0}$=0.900)

Powder batch	$\Delta T_{0.980\text{-}0.900}$ (°C)	$\Delta T_{0.990\text{-}0.900}$ (°C)
A	90.4	148.4
B	99.6	111.6

Declarations

Conflict of interest The authors declare no competing interests.

References

1. Gu DD, Meiners W, Wissenbach K, Poprawe R (2012) Laser additive manufacturing of metallic components: Materials, processes and mechanisms. Int Mater Rev 57:133–164. https://doi.org/10.1179/1743280411Y.0000000014

2. Zhang B, Li Y, Bai Q (2017) Defect formation mechanisms in selective laser melting: A review, Chinese. Aust J Mech Eng. (English Ed) 30:515–527. https://doi.org/10.1007/s10033-017-0121-5

3. Carter LN, Attallah MM, Reed RC (2012) Laser powder bed fabrication of nickel-base superalloys: Influence of parameters; characterisation, quantification and mitigation of cracking. Superalloys 2012:577–586

4. Harrison NJ, Todd I, Mumtaz K (2015) Reduction of microcracking in nickel superalloys processed by selective laser melting: A fundamental alloy design approach. Acta Mater 94:59–68. https://doi.org/10.1016/j.actamat.2015.04.035

5. Shuai L, Wei Q, Shi Y, Zhang J, Wei L (2016) Micro-crack formation and controlling of Inconel625 parts fabricated by selective laser melting, Solid Free. Fabr. Symp. – An Addit. Manuf. Conf 520–529

6. Qiu C, Chen H, Liu Q, Yue S, Wang H (2019) On the solidification behaviour and cracking origin of a nickel-based superalloy during selective laser melting. Mater Charact 148:330–344. https://doi.org/10.1016/j.matchar.2018.12.032

7. Tomus D, Rometsch PA, Heilmaier M, Wu X (2017) Effect of minor alloying elements on crack-formation characteristics of Hastelloy-X manufactured by selective laser melting. Addit Manuf 16:65–72. https://doi.org/10.1016/J.ADDMA.2017.05.006

8. Rappaz M, Drezet J, Gremaud M (1999) A new hot-tearing criterion. Metall Mater Trans A 30:449–455. https://doi.org/10.1007/s11661-999-0334-z

9. DuPont JN, Lippold JC, Kiser SD (2009) Welding metallurgy and weldability of nickel-base alloys. Wiley

10. Shoemaker LE (2005) Alloys 625 and 725: Trends in properties and applications. Superalloys. 718:409–418

11. Carter LN, Wang X, Read N, Khan R, Aristizabal M, Essa K, Attallah MM (2016) Process optimisation of selective laser melting using energy density model for nickel based superalloys. Mater Sci Technol 0836:1–5. https://doi.org/10.1179/1743284715Y.0000000108

12. Mazur M, Benoit M, Easton M, Brandt M (2020) Selective laser melting of Inconel 625 alloy with reduced defect formation. J Laser Appl 32:22058

13. Li S, Wei Q, Shi Y, Zhu Z, Zhang D (2015) Microstructure characteristics of Inconel 625 superalloy manufactured by selective laser melting. J Mater Sci Technol 31:946–952. https://doi.org/10.1016/J.JMST.2014.09.020

14. Marchese G, Garmendia Colera X, Calignano F, Lorusso M, Biamino S, Minetola P, Manfredi D (2017) Characterization and comparison of Inconel 625 processed by selective laser melting and laser metal deposition. Adv Eng Mater. https://doi.org/10.1002/adem.201600635

15. SCANLAB GmbH, SCANLAB RTC5 data sheet, 2017. https://www.scanlab.de/en/products/control-electronics/rtc5

16. ASTM, E8/E8M standard test methods for tension testing of metallic materials 1, Annu. B. ASTM Stand. 4. (2010) 1–27. https://doi.org/10.1520/E0008.

17. Kasperovich G, Haubrich J, Gussone J, Requena G (2016) Correlation between porosity and processing parameters in TiAl6V4 produced by selective laser melting. Mater Des 105:160–170. https://doi.org/10.1016/j.matdes.2016.05.070

18. CIESLAK M (1991) The welding and solidification metallurgy of alloy 625. Weld J 70:49

19. Marchese G, Basile G, Bassini E, Aversa A, Ugues D, Fino P, Id SB (2018) Study of the microstructure and cracking mechanisms of Hastelloy X produced by laser powder bed fusion. https://doi.org/10.3390/ma11010106

20. Chauvet E, Kontis P, Jägle EA, Gault B, Raabe D, Tassin C, Blandin JJ, Dendievel R, Vayre B, Abed S, Martin G (2018) Hot cracking mechanism affecting a non-weldable Ni-based superalloy produced by selective electron beam melting. Acta Mater 142:82–94. https://doi.org/10.1016/j.actamat.2017.09.047

21. Keller T, Lindwall G, Ghosh S, Ma L, Lane BM, Zhang F, Kattner UR, Lass EA, Heigel JC, Idell Y, Williams ME, Allen AJ, Guyer JE, Levine LE (2017) Application of finite element, phase-field, and CALPHAD-based methods to additive manufacturing of Ni-based superalloys. Acta Mater 139:244–253. https://doi.org/10.1016/j.actamat.2017.05.003

22. Deng D, Peng RL, Brodin H, Moverare J (2018) Microstructure and mechanical properties of Inconel 718 produced by selective laser melting: Sample orientation dependence and effects of post heat treatments. Mater Sci Eng A 713:294–306. https://doi.org/10.1016/j.msea.2017.12.043

23. Engeli R, Etter T, Hövel S, Wegener K (2016) Processability of different IN738LC powder batches by selective laser melting. J Mater Process Technol 229:484–491. https://doi.org/10.1016/j.jmatprotec.2015.09.046

24. DuPont JN, Robino CV, Marder AR (1998) Solidification and weldability of Nb-bearing superalloys. Weld J (Miami, Fla) 77:417–431

25. Dubiel B, Sieniawski J (2019) Precipitates in additively manufactured Inconel 625 superalloy. Materials (Basel) 12:1–11. https://doi.org/10.3390/ma12071144

26. Easton MA, Gibson MA, Zhu S, Abbott TB (2014) An a priori hot-tearing indicator applied to die-cast magnesium-rare earth alloys. Metall Mater Trans A 45:3586–3595

27. Yang J, Li F, Wang Z, Zeng X (2015) Cracking behavior and control of Rene 104 superalloy produced by direct laser fabrication. J Mater Process Technol 225:229–239. https://doi.org/10.1016/j.jmatprotec.2015.06.002

28. Cloots M, Uggowitzer PJ, Wegener K (2016) Investigations on the microstructure and crack formation of IN738LC samples processed by selective laser melting using Gaussian and doughnut profiles. Mater Des 89:770–784. https://doi.org/10.1016/j.matdes.2015.10.027

29. Kumar P, Farah J (2019) Influence of processing parameters on properties of Inconel 718. Mater Lett 252:256–259. https://doi.org/10.1016/j.matlet.2019.05.114